The International Journal of Advanced Manufacturing Technology (2022) 119:531–547
https://doi.org/10.1007/s00170-021-08266-x

ORIGINAL ARTICLE

The effect of WAAM process parameters on process conditions and production metrics in the fabrication of single-pass multi-layer wall artifacts

Austen Thien[1] · **Christopher Saldana**[1] · **Thomas Kurfess**[2]

Received: 23 September 2021 / Accepted: 22 October 2021 / Published online: 4 November 2021

Abstract
The present work seeks to understand the impact of varying dwell time and input deposition power on part quality and overall production time for wire arc additive manufacturing. In this work, multi-layer wall geometries were deposited under different input power conditions without affecting the material deposition rate by setting traverse speed and wire feed speed constant and varying the contact tip-to-workpiece distance and the deposition power settings. Current and voltage data and optical imaging of the deposition zone were captured in situ, and wall geometry was characterized using laser scanning, so to understand the applicability of these methods for determining part height in situ. The present results demonstrate that alternating dwell times with lower input deposition power can result in significantly reduced overall production time and minimal material underbuilding, despite increased deposition geometry width. Furthermore, it is shown that while elimination of process dwell results in severe underbuilding of the deposition, it also yields the highest production rate for a hybrid-finished (e.g., deposited, machined) wall in terms of mm in build direction per minute and the highest buy-to-fly ratio.

Keywords Metal additive manufacturing · Wire arc additive manufacturing · Machining · Production metrics

1 Introduction

Additive manufacturing (AM) is a manufacturing technology that is a disruptive technology in the field due to its high production rates and ability to create complex 3D geometries that other manufacturing methods cannot fabricate. An especially prominent AM technology is wire arc additive manufacturing (WAAM) which is typically comprised of a welding system mounted on a machine tool or robotic arm. This method is becoming more standardized due to the familiarity of welding technology coupled with the relatively high material deposition rate. However, one of the drawbacks of WAAM is that the process utilizes a very high heat input rate compared to laser-based additive technologies, and so there needs to be a dwell time, or waiting period, in between each bead or deposition pass. This dwell time accounts for a large share of the deposition time and significantly lengthens the manufacturing process [1]. The dwell time also has a significant impact on the geometry of the part being produced.

The as-deposited bead geometry is governed by two mechanisms: wetting and remelting. Wetting is where most of the deposited material lies on top of the previously deposited bead and is determined by surface tension, much like the wetting behavior of a drop of water on a plate. Remelting is where the previously deposited bead is melted by the heat input of the current deposited bead, and thus, the two molten metals mix. While wetting is the dominant mechanism, both mechanisms are highly dependent on the overall part temperature as surface tension generally decreases with increasing temperature and an increased temperature in the part can lead to a higher degree of remelting [2, 3]. The general effect of increased part temperature on bead geometry is that it causes the deposited bead material to flatten out which, in multi-layer parts, results in shorter and wider geometries than desired and can be seen in multiple studies where part temperature is hotter due to shorter dwell time or the input power is increased [4–6]. Active cooling setups for WAAM systems have been explored in multiple studies to

✉ Austen Thien
athien6@gatech.edu

[1] George W. Woodruff School of Mechanical Engineering, Georgia Institute of Technology, Atlanta, GA, USA

[2] Manufacturing Demonstration Facility, Oak Ridge National Laboratory, Knoxville, TN, USA

decrease part temperature in an effort to create more uniform geometry, but they suffer from being either heavily geometry dependent or impractical to implement in a production environment [7–9]. However, the studies utilizing such devices do show their benefits in maintaining part quality and reducing overall deposition time which even further emphasizes the importance of overall part temperature on part geometry [9–11]. Other studies have utilized a constant long dwell time or a dwell time determined dynamically via in situ temperature monitoring to achieve similar effects [6, 11]. The studies that have varied the input power have done so by varying traverse speed and wire feed speed, which critically alter the material deposition rate and could influence the resulting as-deposited geometry [2, 5].

While the main reason behind the analysis of as-deposited geometry is to ensure that the as-built WAAM parts are conforming to the computer models, another reason is to determine the amount of post-processing that must be completed, since the near net shape parts must be machined to create the net shape component. Variances in as-deposited geometry based on process parameters therefore need to be characterized to better inform the machining process. Several studies have focused on calculating the difference between the total cross-sectional area and the target cross-sectional area in geometric artifacts produced by various process parameters and used that as a metric to determine machining time [5, 12]. Another common metric used is surface waviness, which is the variation in the outline of the cross section of the deposited geometry caused by the different layers stacking on top of each other. Several parameter studies have been conducted where varied sets of process parameters were used to create geometric artifacts and assess their surface waviness with the goal of choosing the process parameters that yield the lowest surface waviness value [2, 13]. While these studies characterize the geometry of WAAM parts with these metrics, those metrics were not used to compute the machining time required. This leads to an incomplete consideration of the variances in artifact geometry in analysis of the overall production process consisting of deposition and post-processing machining operations. Since the machining process does not require lengthy dwell times like the deposition process, it would contribute less to the overall production time, and, thus, there should be less emphasis put on reducing the geometric variances. This means that a WAAM part that is produced with lower dwell times, resulting in larger variances in the part geometry, may not necessarily result in a longer overall production time.

Conventional approaches to geometric analysis of deposited geometry utilize post-production 3D scans or sectioning and polishing to determine part geometry. However, such approaches are inherently slow and are unable to be integrated into closed-loop control systems. It is desirable to establish in situ methods to determine as-deposited bead geometry. While bead width has been primarily determined in situ by using optical cameras [14], the overall part height has been determined in situ using several different technologies. Reisgen et al. [15] have explored using a camera to image the wire electrode, and Xiong et al. [16] utilized a welding camera to determine weld bead height by imaging the melt pool orthogonal to the torch traverse direction. Heralic et al. [17] have utilized a 3D laser line scanner in between successive layers to determine part height. While optical cameras are common in WAAM system setups, process data in the form of arc current and voltage data has also been leveraged to determine part geometry. It is already well documented that changes in the contact tip working distance (CTWD) can significantly affect arc current [18, 19]. Scenetic et al. [20] found the average arc current value for each layer and used that to adjust the increment of the welding torch in the build direction (Z-axis) to effect an in situ method of height control for each layer. Arc current monitoring has also been used to monitor the stability and quality of a WAAM process throughout the build. Aldalur et al. [21] tracked the average arc current for each bead in the fabrication of wall structures to determine change in input energy for oscillating and overlapping deposition strategies. Xia et al. [22] proposed a multi-sensor monitoring framework wherein arc current was monitored via a spectrometer to monitor defects in the welding process.

The present study seeks to understand how part and bead geometry and overall production time are affected by varying input WAAM arc power and dwell time. While previous studies have sought to vary arc power by changes to wire feed speed and traverse speed, this study focuses on modifications to arc power independent of traverse speed and wire feed speed. Additionally, changes in input power are explored through changes to wire electrode length. These changes in input power are paired with changes in dwell time and used to fabricate wall structures as an exemplar part geometry. The process data streams collected in situ and the geometric data collected after fabrication are used to analyze the different fabrication approaches and are assessed as to how viable they are for in situ determination of part height.

2 Methodology

The experimental setup and WAAM parameters used are summarized in Table 1. The WAAM power supply used in this work was operated in power mode, where it behaves like a constant voltage or constant current power supply depending on the current range so to maintain a constant power rating. In this case, the power supply senses the voltage across the circuit and makes small current adjustments to try and maintain constant power. However, since these current adjustments are small, the arc current is still susceptible to

Table 1 Process equipment and parameters

WAAM power supply	**CNC machine**	**Wire material**	**Traverse speed (m/min) [ipm]**
Lincoln Electric MIG Power Wave S500	Cincinnati Dart 500, 3-axis	ER70S-6, 1.2 mm (0.045″) diameter	0.4 [16]
Wire feed rate (m/min) [ipm]	**Initial CTWD (mm) [Z-offset (in)]**	**Initial power setpoints**	**Dwell times (s)**
5.3 [210]	15.2 [0], 21.6 [0.25]	1.5 kW, 2.1 kW	0, 60, and 0/60 alternating

Table 2 Deposition geometry parameters

Layer height (mm)	Number of layers	Expected height (mm)	Desired width (mm)	Wall length (mm)
2.03	20	40.64	6.35	152.4

Table 3 Experimental test conditions

Experiment	P_0 (kW)	$CTWD_0$ (mm)	Interlayer dwell strategy	Dwell time (s)
1	2.1	15.2	Constant	60
2	1.5	15.2	Constant	60
3	2.1	21.6	Constant	60
4	2.1	15.2	None	0
5	1.5	15.2	None	0
6	2.1	21.6	None	0
7	2.1	15.2	Alternating	0, 60
8	1.5	15.2	Alternating	0, 60
9	2.1	21.6	Alternating	0, 60

employed including no interlayer dwell (0 s), constant interlayer dwell (60 s), and alternating interlayer dwell where the dwell time alternated between 0 and 60 s between layers. The geometry chosen for this study was a straight wall geometry with dimensions summarized in Table 2. The path planning for the wall consists of alternating the start point of the deposition to opposite ends of the wall in successive layers so to minimize build-up of material at one end of the wall, which is common practice for metal AM. Table 3 lists the experiments conducted for this study. Each parameter set was used to fabricate the target geometry. Experiments 1, 4, and 7 used nominal P_0 and nominal $CTWD_0$. Experiments 2, 5, and 8 were designed to understand effect of lower P_0. Experiments 3, 6, and 9 were designed to understand effects of increased $CTWD_0$.

The in situ process data collected were the current, the voltage, and the CTWD. A Jetson Nano microprocessor was connected to the WAAM power supply to sample current and voltage data at 10 Hz. This data was then passed on to a BeagleBone Black microprocessor which transmitted the data over an MQTT broker to a cloud-based SQL database. Current and voltage data for a test bead can be seen in

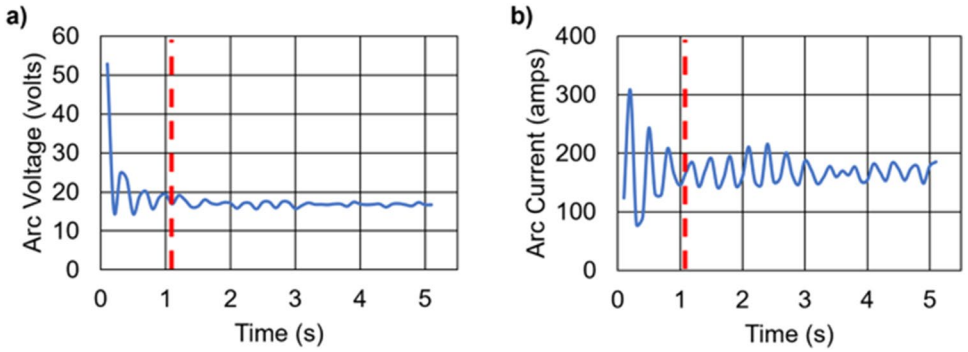

Fig. 1 **a** Measured voltage and (**b**) current, for example, deposition, using traverse speed and wire feed speed from Table 1. Red line indicates switchover to stable arc performance

larger changes caused by variations in the wire CTWD. The deposition head was mounted on a 3-axis CNC machine in the spindle using a standard CAT40 tool holder.

The initial CTWD lengths, notated as $CTWD_0$, were chosen as a nominal value (15.2 mm) and an increased value (21.6 mm) so to limit changes in shielding gas coverage. The initial power setpoints, notated as P_0, chosen were 2.1 kW (nominal) and 1.5 kW. For dwell time, three strategies were

Fig. 1. The portion of the wave form with the large variations in amplitude prior to 1.25 s represents the arc formation where an arc is being established, and the lower amplitude region after 1.25 s represents the stable arc portion of the waveform.

The actual measured CTWD, notated as $CTWD_a$, data was gathered by imaging the deposition process using a

Basler a2A1920-160ucBAS optical camera with a neutral density filter. This camera was attached to the spindle housing of the CNC machine and moved with the WAAM deposition head. The method to image CTWD length is similar to that used by Riesgen et al. [15], where the stick-out, or the length of wire protruding from the gas nozzle, was determined from the optical camera image. In the present study, the centroid of the arc was used as the stick-out value and was found from the initial optical camera image by first creating a binary image through thresholding. Then, the arc was found via a blob detection method, where the centroid values were used for $CTWD_a$. Since the camera was attached to the same rigid frame as the deposition head, changes in the centroid location corresponded to changes in $CTWD_a$. Figure 2 shows an example detection of the blob centroid to determine $CTWD_a$.

After the walls were fabricated, they were scanned by a FARO Blue Laser Line Probe attached to a FARO robotic arm. The point clouds gathered by the scanner were then converted to a watertight.STL using Geomagic software. The FARO scans of the completed walls were processed in several stages. A special Python library was used to slice each.STL and extract the point cloud data for that slice. The extracted slice can be seen in Fig. 3a and the cropping

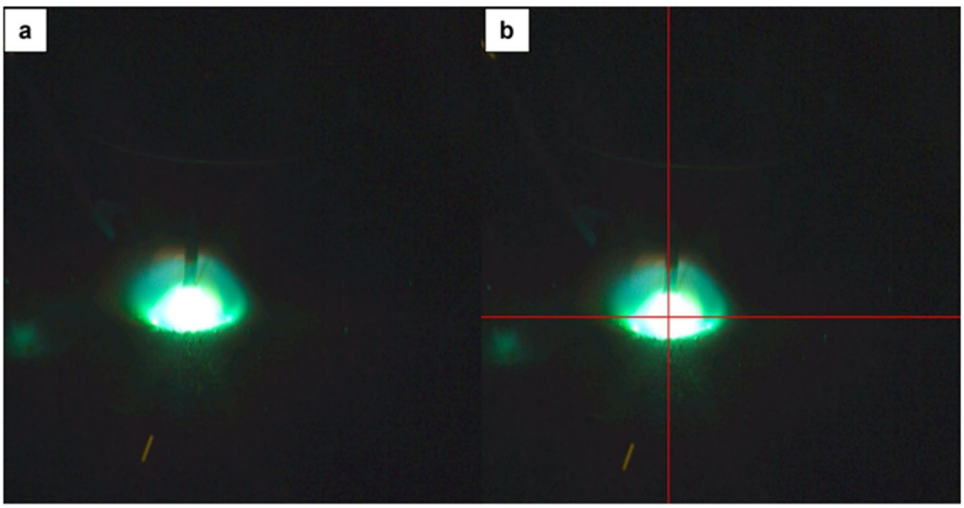

Fig. 2 **a** Unprocessed optical camera image and (**b**) determination of deposition centroid

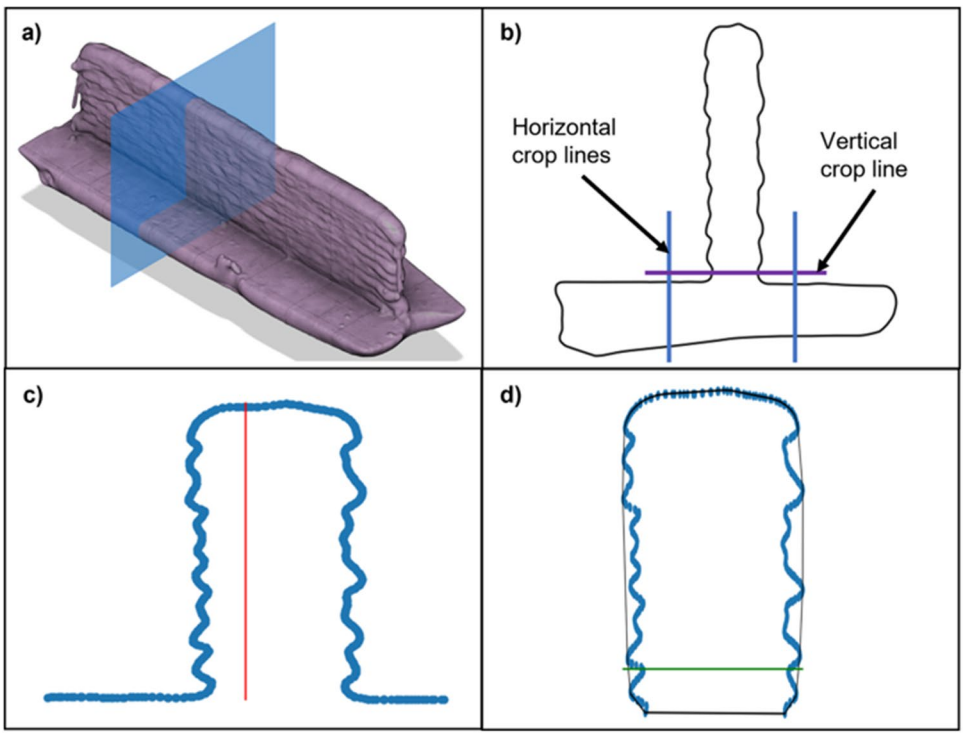

Fig. 3 **a** Scan geometry of deposited wall (.STL model), (**b**) cropping from scan geometry, (**c**) calculation of deposition height, and (**d**) convex hull determination and calculation of deposition width

operations in Fig. 3b. The first cropping operation, designated by the blue lines, was used to show the wall profile and the surrounding build plate edge. This allows for the wall height to be calculated as shown in Fig. 3c by the vertical red line. The second cropping operation, designated by the purple line, was used to isolate the wall profile. That isolated wall profile was then used to generate a convex hull from which the maximum wall width for that slice could be calculated, as shown in Fig. 3d. The height and width for each wall slice were calculated using slices spaced every 5 mm along the length of the wall.

3 Results

3.1 Wall artifacts

A side view of the as-deposited wall artifacts for each of the experiments is provided in Fig. 4. Note that there are some observable localized variations in the wall geometry at the end points of the wall (blue arrows), which are to be expected as the start and stop points of each bead typically have larger material build-up than the rest of the weld bead. This in turn causes the material flow at the start and stop points to be more unpredictable and results in varied wall geometry. Other aberrations in the experiments can be seen in Fig. 4a and e, where there are localized depressions (green arrows) in the mid-length of the top surface. These localized depressions occur when there are temporary arc failures in the deposition process, as the WAAM power supply will stop feeding wire until an arc is re-established but the CNC machine tool still traverses the torch, which results in a gap in the bead geometry. Additionally, experiment 6 experienced significant process issues and is discussed in the ensuing.

3.2 In situ process data

The in situ process data is summarized according to dwell time in the ensuing as this corresponds to similar heat dissipation condition (e.g., dwell time) while varying the heat input condition (e.g., power). The current, actual power P_a, voltage, and $CTWD_a$ evolved for the 60-s dwell time experiments are shown in Fig. 5. Figure 5a clearly shows differences in measured current for the different process parameter sets. At a constant $CTWD_0 = 15.2$ mm, the effect of deposition power is seen in the measured current, voltage, and P_a. For lower $P_0 = 1.5$ kW, this resulted in similar measured current of 170–180 A, but noticeably lower arc voltage and arc power compared to $P_0 = 2.1$ kW. As $CTWD_0$ increased to 21.6 mm, this resulted in a measured arc current 20 A lower and a measured arc voltage 1.5–2 V higher than in the nominal $CTWD_0$ condition. Further, P_a decreased by 150 W. In terms of effects of the processing parameters on $CTWD_a$, it was observed that higher P_0 resulted in a marked increase in $CTWD_a$ by ~ 3%.

Figure 6 shows the same in situ process measurements with no dwell time applied between deposited layers.

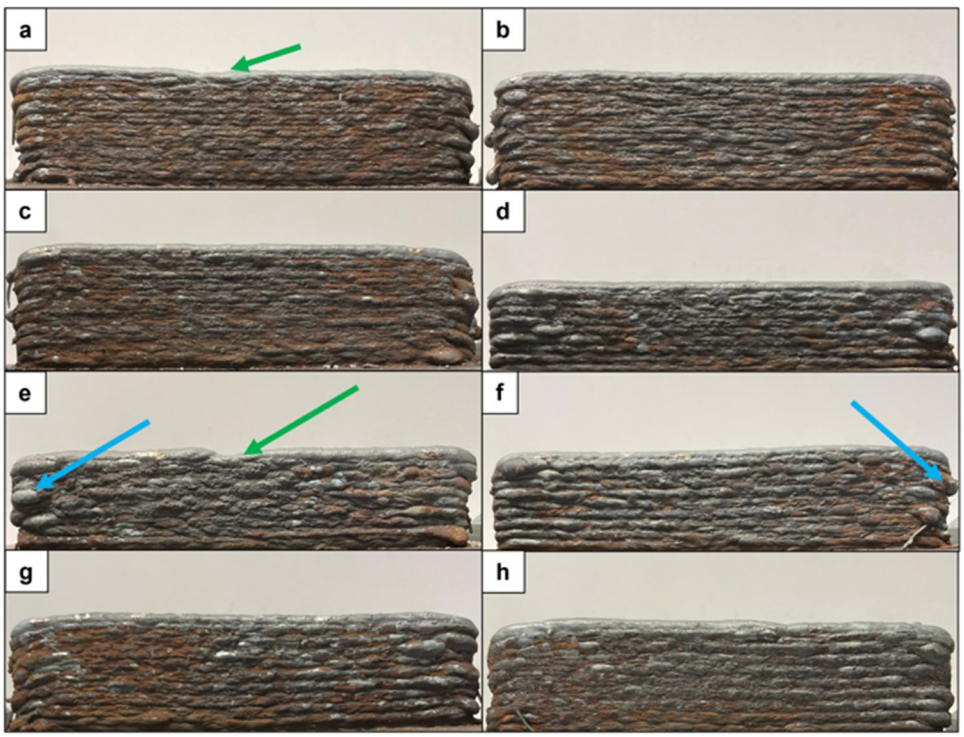

Fig. 4 Side views of as-deposited wall artifacts from (**a**) experiment 1, (**b**) experiment 2, (**c**) experiment 3, (**d**) experiment 4, (**e**) experiment 5, (**f**) experiment 7, (**g**) experiment 8, and (**h**) experiment 9

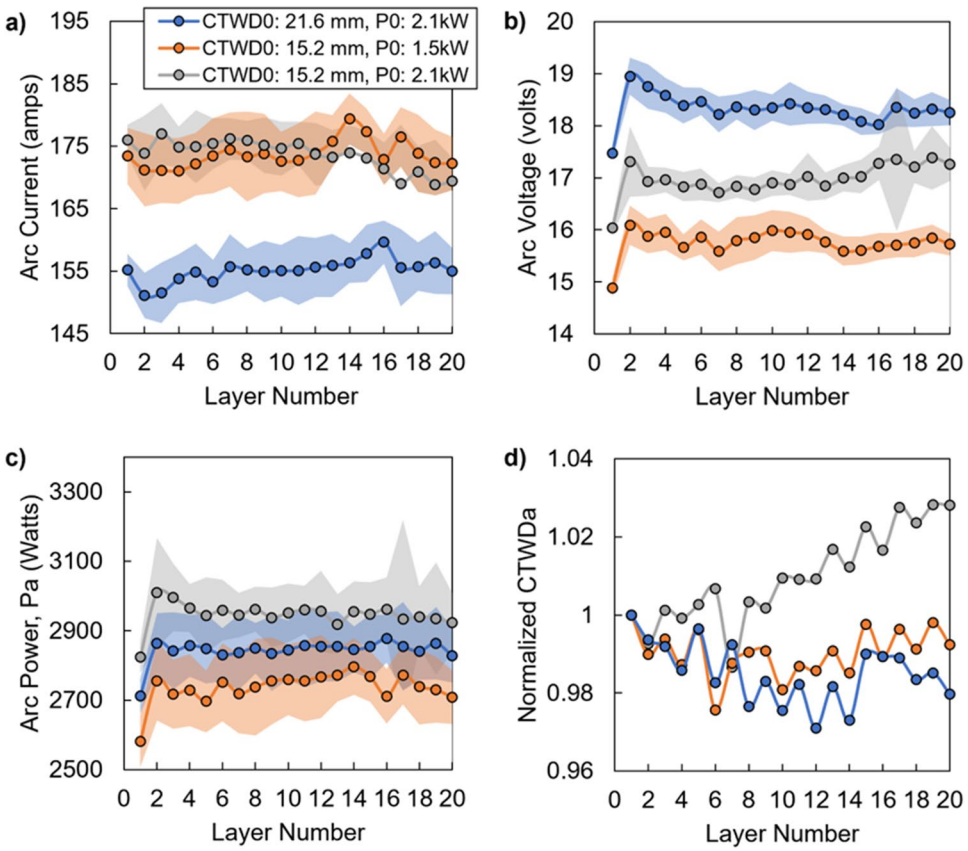

Fig. 5 Data for 60-s interlayer dwell: (**a**) current, (**b**) voltage, (**c**) P_a, and (**d**) $CTWD_a$

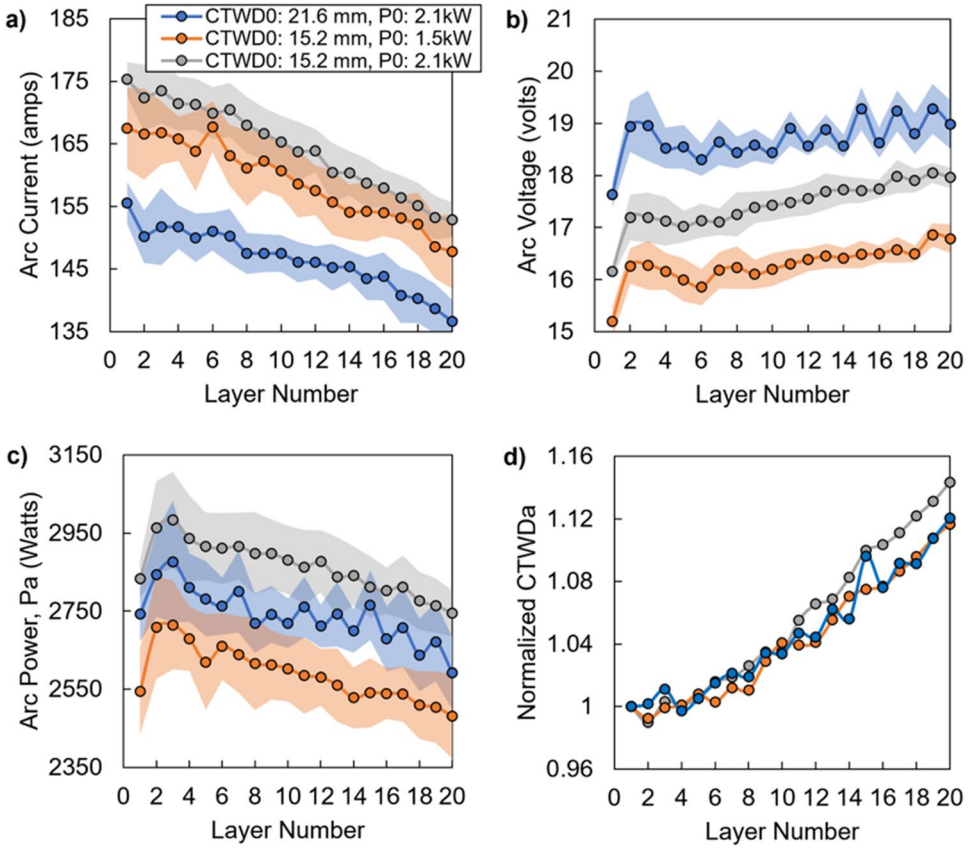

Fig. 6 Data for no interlayer dwell: (**a**) current, (**b**) voltage, (**c**) P_a, and **d** $CTWD_a$

In this case, the measured arc current, voltage, and P_a exhibited similar behavior in terms of the effect of P_0 and $CTWD_0$. Specifically, the following were observed with an increase in $CTWD_0$ to 21.6 mm at a constant P_0: (1) measured arc current was seen to decrease significantly by 20 A, (2) measured arc voltage increased by 1–2 V, and (3) P_a decreased by 150 W. Additionally, the following were observed with an increase in P_0 from 1.5 to 2.1 kW at constant $CTWD_0$: (1) slight increase in measured current by 5–10 A, (2) increase in measured arc voltage by 1 V, and (3) increase in P_a by 250 W. One salient difference between these measurements compared to the experiments conducted with an interlayer dwell time of 60 s is the non-steady nature of these measured current, voltage, and P_a data as a function of layer. In this case, these have clear decay in the case of arc current and P_a and an increase in arc voltage as layers increase to 20 throughout the build. Further, $CTWD_a$ is found to increase for all conditions by as much as 12–15% over $CTWD_0$.

Figure 7 shows the effects of an alternating dwell time on the in situ process measurements. As can be seen in the figure, the relative changes in measured arc current, arc voltage, and P_a followed similar general trends as in the case of a constant 60-s dwell time and a condition with no dwell time. However, one noticeable difference in this case was better control of the variation in normalized $CTWD_a$ with a peak deviation of 8% across the 20-layer build.

3.3 Wall geometry data

The wall geometry of the as-deposited wall artifacts is presented in Fig. 8. Slices of the.STL were taken every 5 mm along the length of the wall, and the width of the wall was calculated at 1-mm increments along the height of the wall in each slice. The average wall width from all slices at each height increment is then used to plot a width profile that displays how the average wall width changes along the height of the wall for each artifact. The transparent shaded bands in Fig. 8 represent the standard deviation of the width measurement. The decrease in width shown at the top of all artifacts is due to the curvature of the top bead of the wall. The effect of dwell time and strategy on the as-deposited geometry is clear from the figure. With no interlayer dwell, Fig. 8d, e, and f show that the as-deposited wall width increased along the wall height by approximately 3–4 mm and had a maximum standard deviation ranging from approximately 1.3 to 2.9 mm. Figure 8a, b, and c show that as interlayer dwell was set at a constant 60 s, the as-deposited wall width increased slightly by approximately 0.5–1.4 mm and has a maximum standard deviation ranging from approximately

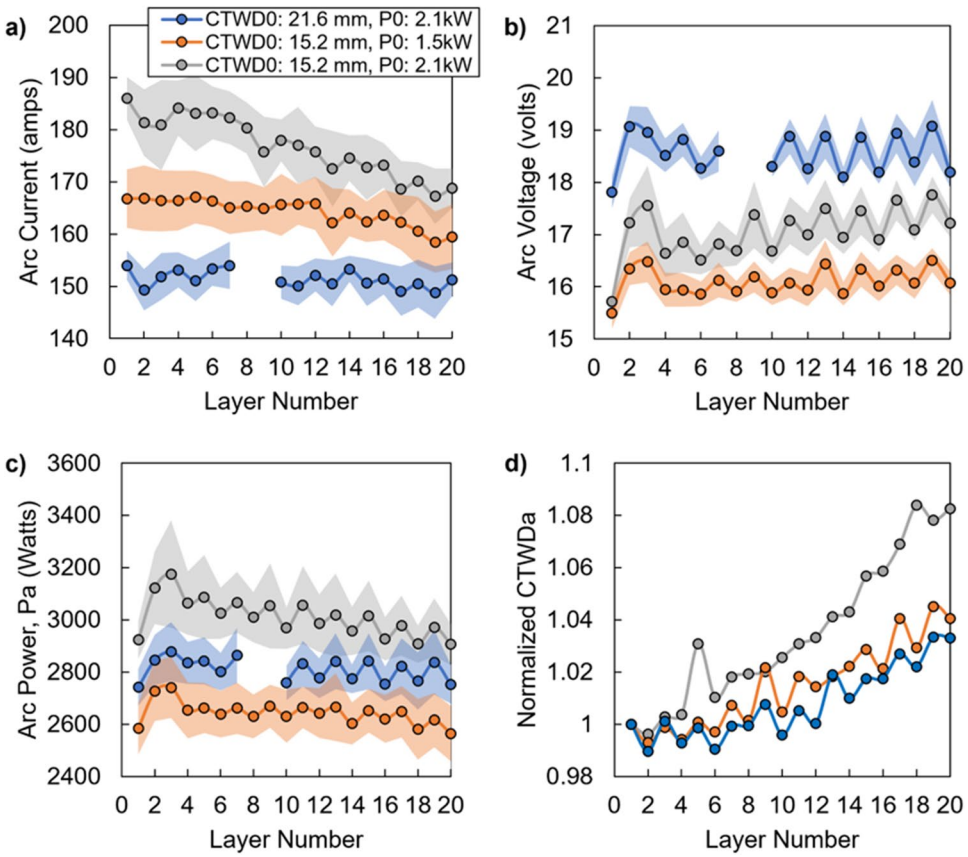

Fig. 7 Data for alternating interlayer dwell (0 s, 60 s): (**a**) current, (**b**) voltage, (**c**) P_a, and (**d**) $CTWD_a$

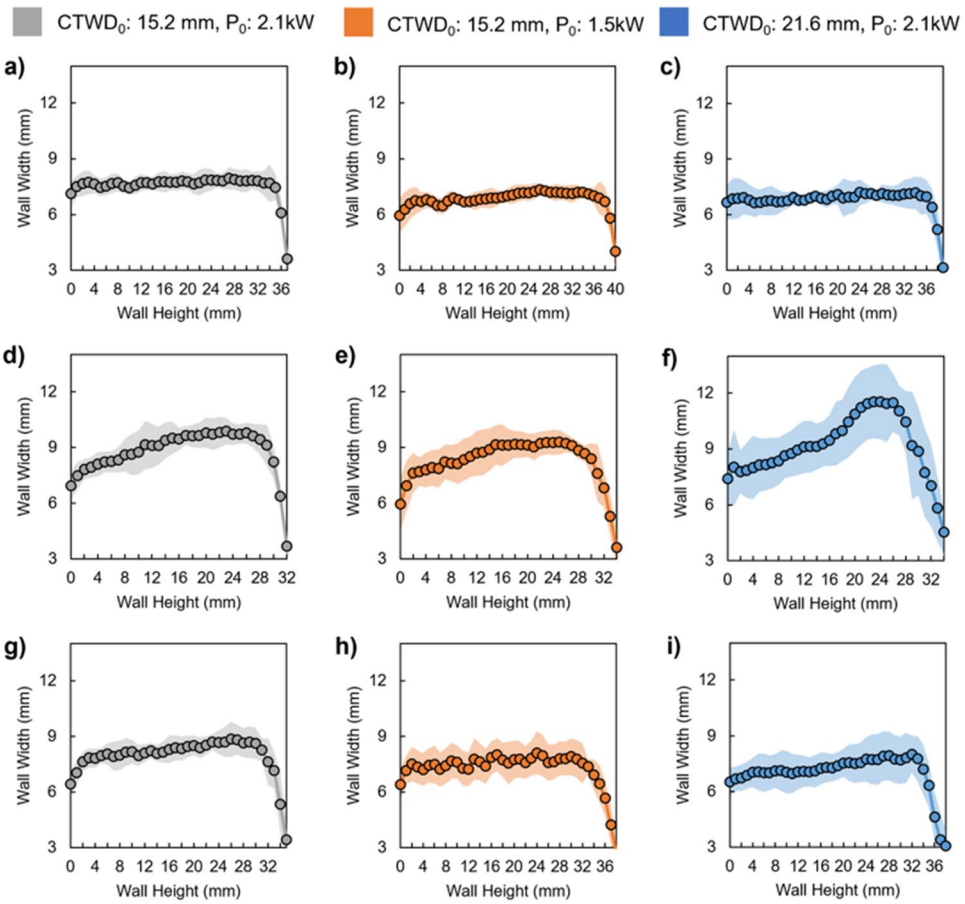

Fig. 8 Width profiles of as-deposited wall artifacts from (**a**) experiment 1, (**b**) experiment 2, (**c**) experiment 3, (**d**) experiment 4, (**e**) experiment 5, (**f**) experiment 6, (**g**) experiment 7, (**h**) experiment 8, (**i**) experiment 9. Shaded regions indicate error bands of standard deviation

0.9 to 1.1 mm. Lastly, when a varying interlayer dwell strategy that alternates between 0 and 60 s was used, Fig. 8g, h, and i show that the as-deposited wall width increases by approximately 1.4 to 2.4 mm and has a maximum standard deviation 1.2–1.6 mm.

To compare the as-deposited geometry to the target geometry, average measurements for the height and width of each wall artifact are shown in Fig. 9 relative to the target geometry. The effect of dwell time and strategy on the as-deposited geometry is again clear from the figure. The as-deposited wall artifact height of the 0-s interlayer dwell condition was between 33.00 and 35.50 mm, which is far below the target height of 40.64 mm. Further, the as-deposited wall artifact width ranges from 10.50 to 13.50 mm, which is far greater than the 6.35-mm target width. As interlayer dwell time was set constant at 60 s, the as-deposited geometry was

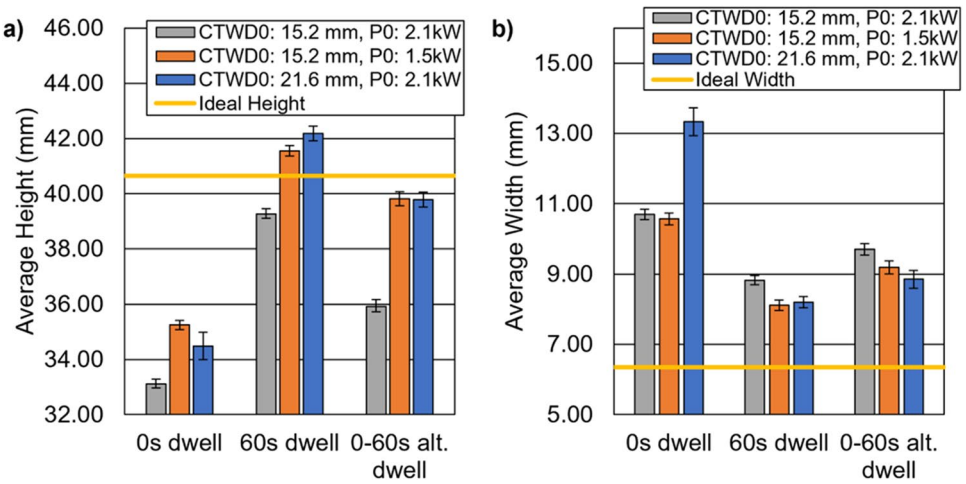

Fig. 9 Measured as-deposited geometry (**a**) height and (**b**) width as a function of dwell time and deposition parameters

substantially closer to that of the target values, with a height ranging from 39.00 to 42.00 mm and a width ranging from 8.00 to 9.00 mm. With an alternating dwell strategy with interlayer dwells varying between 0 and 60 s, this resulted in an as-deposited accuracy better than that of a no-dwell strategy and a constant 60-s dwell. Of particular interest is the case with no interlayer dwell, $CTWD_0 = 21.6$ mm and $P_0 = 2.1$ kW, which resulted in an as-deposited bead width of more than 13.00 mm. In this case, there were some significant build failures during deposition. As shown by the 3D scan in Fig. 10a, there was deposited material that flowed from the intended deposition surface and solidified at the base of the build plate. Additionally, Fig. 10c and d show that there are build failures in this wall artifact that resulted in large porosity and highly variable wall height. These build failures can be attributed to inadequate shield gas coverage due to the increased $CTWD_0$ being compounded with the inherent instability of $CTWD_a$ seen in the 0-s dwell time in Fig. 6.

3.4 Production time

Critical to the complete fabrication of components by WAAM is the impact of errors in the deposition on subsequent machining. In this case, the overall production time comprises both the deposition time (including dwell times) and the machining time, where error due to overdeposition must be accommodated by additional machining time. In the ensuing analysis, we consider the machining time to include the time needed to machine the as-deposited widths to the desired value. The machining parameters used were a surface speed of 205 m/min, tool diameter of 15.875 mm, feed rate of 0.1 mm/rev, and radial depth of cut of 0.26 mm.

The overall production time as a function of deposition condition is summarized in Fig. 11. From the figure, it is clear that the 0-s dwell time experiments had the lowest production time, followed by the 0- or 60-s alternating dwell time experiments and then the 60-s dwell time experiments. The 60-s dwell time and 0- or 60-s alternating dwell time experiment sets had maximum deviations in overall production time of approximately 45 s, and the 0-s dwell time experiment set had a maximum deviation of approximately 220 s, although this was due to the build defects in experiment 6 explained earlier.

4 Discussion

Multiple streams of in situ process data were collected in this work with the object of tracking the overall height of the part. The direct measurement of the welding camera to determine $CTWD_a$ provides an obvious method to find the part height, but that type of data stream may not always be available. Thus, it would be advantageous to analyze the other data streams to determine their viability. The in situ process data graphs indicate that the arc current value could

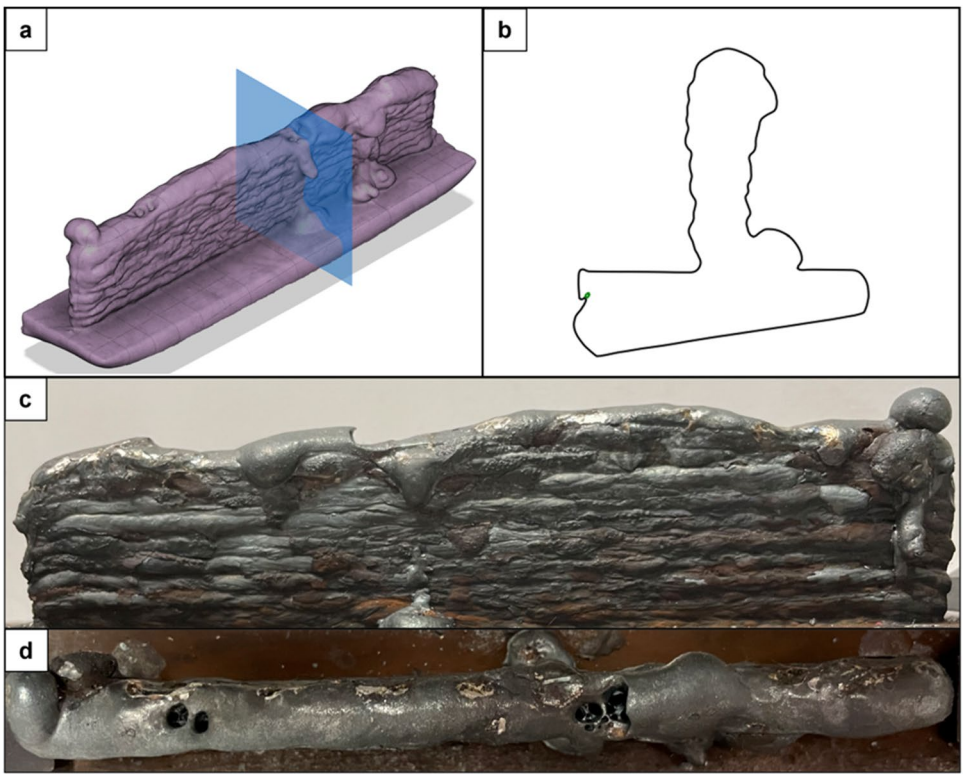

Fig. 10 Experiment 6 build quality including (**a**) isometric view with section plane, (**b**) corresponding cross-sectional geometry, (**c**) as-deposited build side view, and (**d**) build top view

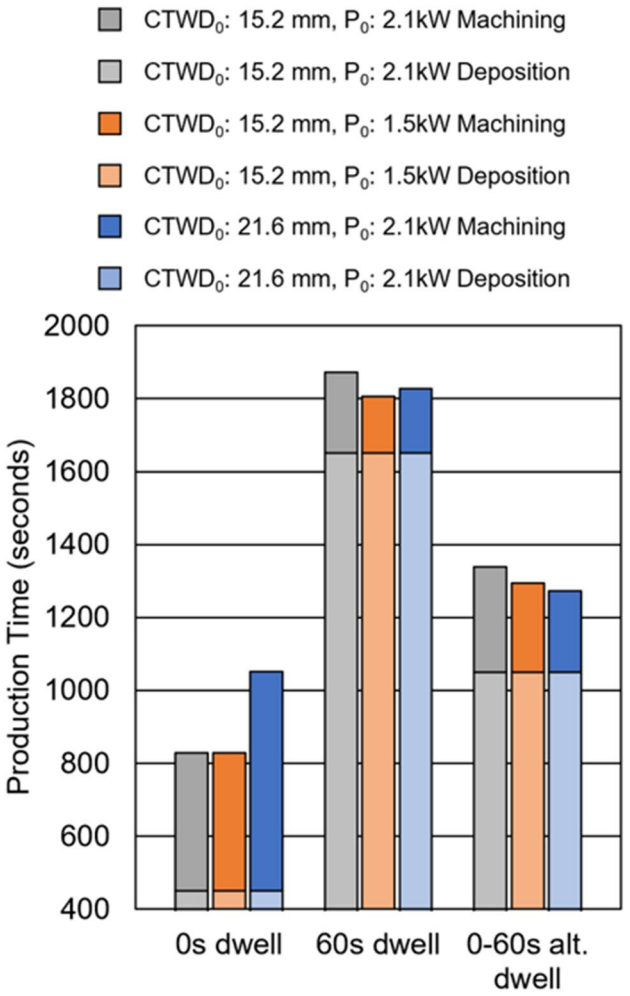

Fig. 11 Overall production time of wall experiments

be a better indicator of $CTWD_a$ than arc voltage. While both the arc voltage and arc current curves for individual experiments show approximately linear trends following the changes in $CTWD_a$ according to Ohm's law, there are some distinct differences that can be seen when comparing the arc current and arc voltage curves among experiments using different process parameter sets. When comparing the arc current and arc voltage curves shown in Fig. 5a and b for experiments 1 and 3, which utilize a $CTWD_0 = 15.2$ mm and a $CTWD_0 = 21.6$ mm, respectively, and the same $P_0 = 2.1$ kW setting, the arc current decreases by approximately 11.4%, while the arc voltage only increases by 5.9%. This shows that the arc current is more sensitive to increases in $CTWD_a$ than the arc voltage. Additionally, the same arc current and arc voltage graphs of the 60-s dwell time experiment set in Fig. 5a and b show that for experiments 1 and 2, which utilize $P_0 = 2.1$ kW and $P_0 = 1.5$ kW, respectively, and the same $CTWD_0 = 15.2$ mm, the arc current values differ by approximately 3.4%, whereas the arc voltage values differ by approximately 9.1%. This further supports the notion that arc current is more sensitive to changes in $CTWD_a$ as the voltage value was altered to achieve the needed power differential instead of the current.

Additionally, it can be seen in Figs. 5b, 6b, and 7b that the voltage value for the first layer is significantly lower than that of the subsequent layers by as much as 9% in some experiments. This is because at the beginning of the deposition process, the build plate is at room temperature and thus has a lower resistance value than later when the build plate and part are much hotter [18, 23]. Since the object of collecting this data is to determine the overall part height by calculating the change in the process parameter from the parameter's first layer value, using voltage data in this way would skew the results. Furthermore, in Fig. 7a and b for the 0- or 60-s alternating dwell, the voltage value oscillates, but the current value does not. The oscillation in the voltage curve can be attributed to the alternating dwell times which leads to an increased heat build-up every other layer. This can cause changes in the resistance and therefore changes in the voltage value. This oscillation only results in a maximum deviation of 4.7% but is still significant when considering percent change in voltage value from the first layer.

Since it has been established that the current and weld camera images are the best data streams to determine part height in situ, a comparison to the high-fidelity geometric data from the 3D scan of the part is needed. Figure 12 shows the percent changes in the arc current, $CTWD_a$, and overall part height determined from the 3D scan data for each of the experiments. Note that the arc current and $CTWD_a$ percent change is calculated between the first and last layers, whereas the overall part height data is calculated as the percent change between the average wall height value and desired height value. For clarity, both positive and negative values are shown on the same vertical axis, with the bars that are outlined in black representing a negative value. Ideally, a decrease in the scan height should be paired with in an increase in the $CTWD_a$ and a decrease in the arc current from the extended wire, and vice versa for an increase in scan height. Overall, the trends match each other well with the expected direction of the percent change in the data streams. The only deviations from this trend are in experiments 2 and 3 where the 3D scan height and $CTWD_a$ percent changes match in direction but the arc current percent change does not. Since the scan height increased and the $CTWD_a$ decreased in experiments 2 and 3, it is expected that the arc current should increase due to the shorter wire having less resistance. However, the arc current percent change is only slightly negative: −0.67% and −0.13% for experiments 2 and 3, respectively. This deviation from the trend could be a result of noise in the signal caused by the dynamic changes in current from arc formation seen in Fig. 1. The largest percent change in the arc current and $CTWD_a$ occurs for the

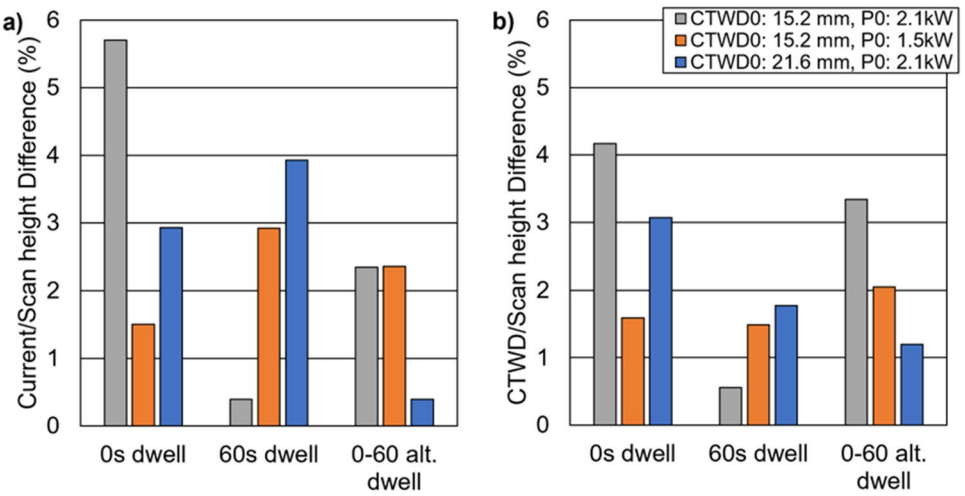

Fig. 12 Height measurement comparison. (**a**) Difference between current and scan height, (**b**) difference between $CTWD_a$ and scan height

0-s dwell time, followed by the 0- or 60-s alternating dwell time, and finally the 60-s dwell time and this trend are seen for all process parameter sets in Fig. 12. This means that the least stable processes are when the 0-s dwell time is used. The difference between the arc current and 3D scan height percent changes ranges from a minimum of 0.39% and a maximum of 5.7%, while the difference between the $CTWD_a$ and 3D scan height percent changes ranges from a minimum of 0.56% and a maximum of 4.17%.

The experiments conducted in the present work produced walls with average widths that range from 8.12 to 10.70 mm. These are within the boundaries of the process window explored by Ding et al. [24] who reported single bead width extremes of approximately 3 to 11 mm when using mild steel. While this confirms that the wall widths achieved are reasonable for the WAAM process and material used, Ding et al. [24] carried out their single bead experiments by varying traverse speed and wire feed speed and furthermore did not characterize bulk wall width. The closed-loop bead width control methodology explored by Xiong et al. [14] did characterize bulk wall width in an artifact made from H08Mn2Si mild steel wire where wall width was varied in 1-mm steps from approximately 6 to 10 mm. These comparisons show that the range in width seen in the results of this study is within the established process norms.

The present work sought to vary the heat input and accumulation conditions during the production of wall artifacts, and so comparisons must be made to the work of other researchers who took this approach. Kozamernik et al. [11] explored the effect of dwell time and active cooling via compressed air on 16-layer, 70-mm-long wall artifacts made with G3Si1 mild steel wire and reported that there were only small differences in the wall heights and widths (~0.1 mm and ~0.3 mm, respectively) between the interpass temperature controlled and constant dwell time conditions. While this contrasts markedly from the wall width results reported in the present work, it should be noted that the wall artifacts in the Kozamernik study were about half of those used in the present work. Additionally, Kozamernik et al. [11] reported using current and voltage settings of 66 A and 14.4 V which can be seen to be much lower than those used in the present work. Both differences have the effect of a much lower heat input which in turn would result in much lower changes in bull wall geometry. Another study by Xiong et al. [25] reported that increasing interpass temperature in the construction of 20-layer, 160-mm-long walls using H08Mn2Si mild steel wire resulted in a decrease in average layer height. Based on those reported results, and the fact that the average layer height was calculated over the top 15 layers, the change in bulk height from the lowest to the highest interpass temperature condition can be estimated to be approximately ~3 mm. This height discrepancy is less than half what was reported in the present work, but this difference can be explained by the fact that Xiong et al. [25] used a lower wire feed rate (3.73 m/min as opposed to 5.3 m/min used in the present work) which resulted in a lower current and thus a lower heat input that caused the deposited beads to be taller. The effect of the increased $CTWD_0$ on the bulk wall geometry can also be compared to previous work. Henckell et al. [19] found that increasing $CTWD_0$ resulted in taller and thinner wall artifacts when using G4Si1/SG3 wire and reported that using a CTWD of approximately 20 mm to build a 10-layer, 100-mm-long wall artifact resulted in a bulk wall width of approximately 7 mm. The present work utilized a process condition of a $CTWD_0$ that was approximately 21.6 mm which resulted in a bulk wall width of 8.2 mm for the conservative dwell time condition. This discrepancy can be explained by the fact that the present work used a wire feed rate of 5.3 m/min as opposed to the 5 m/min used by Henckell et al. [19].

Other researchers have conducted similar studies utilizing different material systems. The research conducted by

Lee et al. [12] reported that decreasing the interpass dwell time in the production of 10-layer, 100-mm-long walls with M-316L stainless steel wire resulted in a lower effective area ratio and that the top layers of the wall artifact are wide and short due to increased heat accumulation. This same effect can be seen in the wall artifact cross sections for the present work, but since Lee et al. [12] did not report any wall width values for their study, no trend comparison can be made to the wall width results of the present work. Kohler et al. [6] reported that increasing the interpass dwell time in the production of 140-mm-tall, 300-mm-long artifacts using Al-5356 wire resulted in a decreased in wall width by ~ 11–13%. This trend is mirrored in the present study but more severely as the walls produced with 0-s dwell time are ~ 17–23% thicker than walls produced with 60-s dwell time for both the P_0 and $CTWD_0$ conditions. Lastly, both Wang et al. [10] and Li et al. [8] reported that the use of active cooling techniques in building wall artifacts with Al–Mg wire resulted in wall width reductions of ~ 13.8% and ~ 22.4%, respectively.

As mentioned in the "Results" section earlier, experiments 2 and 3 have comparable wall widths but differ in wall height by 0.63 mm with experiment 3 being the larger. These discrepancies in wall height and width can be explained by the differing P_0 and $CTWD_0$. Experiment 3 has an increased $CTWD_0$ which leads to a decreased arc current, as shown by Fig. 5a. This decrease in arc current leads to a corresponding decrease in weld penetration since it is well documented that arc current is the most significant factor on weld penetration [18, 26]. The decrease in weld penetration means that less material is being melted into the preceding layer which then results in a taller bead. Experiment 2 has a nominal $CTWD_0$ which results in a higher arc current, as seen in Fig. 5a, as well as a higher weld penetration. This ultimately results in a shorter weld bead since more material is melted into the preceding layer. The reason that the widths of experiment 2 and 3 are comparable could be that the extended dwell time allows for enough heat dissipation so that the surface tension of material being deposited is approximately equal. Conversely, experiments 8 and 9 have comparable heights but their widths only differ by 0.34 mm. Experiment 9 also has an increased $CTWD_0$ leading to a decreased arc current, as shown by Fig. 7a, and a decrease in weld penetration. However, in experiment 9, there are alternating dwell times causing lower heat dissipation. This leads to less surface tension and therefore increased wetting of the deposited material which counteracts the effects of the decreased weld penetration and causes a wider and shorter bead than experiment 3.

In previous research in the WAAM field, there has been as much consideration given to the effect of machining operations on the overall production time estimation for WAAM. Fuchs et al. [13] give an equation for determining the amount of machining allowance needed to overcome deposition inaccuracies when constructing oscillating wall structures out of Ti-6Al-4 V wire for different deposition process parameters, but their study does not comment on tradeoffs between deposition time and machining time and how the two operation times influence the overall production time. Yehorov et al. [5] discusses a methodology whereby, based on a desired wall width, an optimal range of traverse speeds can be selected to minimize deposition time and the surface waviness, which indicates the amount of excess material that must be removed. However, the machining times were not incorporated into the analysis, so the production rate for a fully deposited and post-processed artifact could not be discerned. Furthermore, the relationship between the deposition time and machining time for wall artifacts built with different process parameter and dwell time strategies could not be explored.

In the present work, the amount of overall production time devoted to machining also changed depending on the dwell time, with the 0-s dwell time experiment set using 378–600-s machining time, the 0- or 60-s alternating dwell time experiment set using 222–289-s machining time, and the 60-s dwell time experiment set using 155–222-s machining time. At first glance, the increased machining time and lower average wall height for the 0- or 60-s alternating and 0-s dwell time trials would suggest that these are unacceptable manufacturing methods since they are underbuilt and would require more post-processing. However, this conclusion is based on the assumption that the desired geometry needs to be manufactured in one deposition and one machining step. But if one instead assumes that the desired geometry could be built in multiple deposition and machining steps, then the manufacturing considerations would change greatly. To further this analysis, the production time and wall geometry data can be reformulated to express the production rate in finished part height per unit time. This metric divides the average wall height from Fig. 9a and divides it by the overall production time, including deposition and machining, from Fig. 11 and can be seen in Fig. 13a. The finished wall production rate for the 0-s dwell time trials is the fastest at 2–2.5 mm/min, followed by the 0- or 60-s alternating dwell time trials at 1.6–1.88 mm/min, with the 60-s dwell time trials being the slowest at 1.26–1.38 mm/min. These results emphasize that the production mentality shifts from depositing the calculated number of layers while minimizing the amount of machining to continuously depositing layers until the desired wall height is reached while accepting larger increases in the amount of machining time needed. However, the increased $CTWD_a$ caused by the lower dwell times can lead to issues with shield gas coverage that can in turn cause porosity, as seen in Fig. 10, so adaptive control measures should be taken to reset the $CTWD_a$ periodically throughout the build.

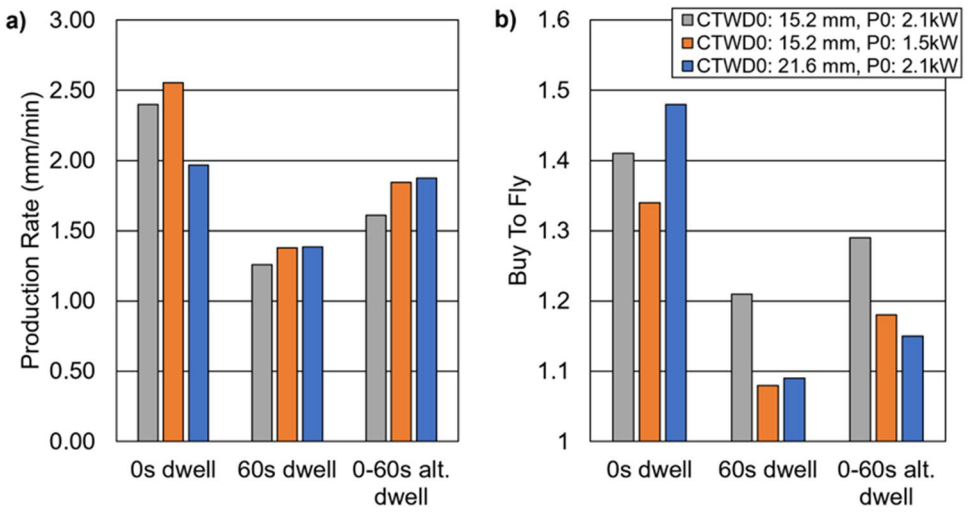

Fig. 13 As-deposited wall artifact production data: (**a**) finished wall production rate and (**b**) buy-to-fly ratio

Another important production metric is the buy-to-fly ratio (BTF), which is a measure of the material waste from a production process and is calculated as the ratio of the weight of material deposited to the weight of net shape material produced [27]. As seen in Fig. 9b, the experiment sets with 0-s and 0- or 60-s alternating dwell times have lower wall heights which in turn cause increases in the BTF since the amount of net shape material produced is lower but the amount of material deposited is the same. Figure 13b shows that the trend of the BTF among the different dwell time conditions roughly mirrors the finished wall production rate trend, with the 60-s dwell time trials having BTFs of 1.08–1.21, the 0-s dwell time trials having BTFs of 1.34–1.48, and the 0- or 60-s alternating dwell time trials having BTFs of 1.15–1.29. Another interesting trend seen in Fig. 12b is that the nominal process parameter trials (Z0.0, 2.1 kW) seem to have large BTF values for all dwell time conditions except the 0-s dwell condition, but this aberration can be attributed to the poor build quality of experiment 6.

The data shown in Fig. 13 suggest that there is a trade-off between finished wall production rate and BTF among the different dwell time conditions. However, the metrics of finished wall production rate and BTF in Fig. 13 were calculated considering average values of the as-deposited wall artifact geometry. In actuality, as shown in Fig. 8, the width of the wall artifacts increases as the wall height increases. This means that the cross-sectional area of the wall artifacts along the wall height will be different for artifacts built using different interlayer dwell time strategies. Figure 14 shows area graphs of each wall artifact with the vertical width axis being truncated at 3.18 mm (half of the target width 6.35 mm) to illustrate the excess area that needs to be machined off each wall artifact in order to reach the target width. The increases in excess area along the wall height mimic the trends seen in Fig. 8. Figure 14a, b, and c show that the wall artifacts built with a 60-s interlayer dwell have the least increases in excess area, Fig. 14d, e, and f show that the wall artifacts built with a 0-s interlayer dwell have the most increases in excess area, and Fig. 14g, h, and i show that the wall artifacts built with the alternating interlayer dwell strategy have excess area increases between those of the wall artifacts made with the 60- and 0-s interlayer dwell strategies.

5 Case Study

The phenomenon shown in Fig. 14 and described in the previous paragraph means that the important metrics of production time and BTF ratio are dependent on the wall height. Therefore, when employing an incremental deposition and machining build strategy, rather than a wholesale deposition and machining build strategy as described earlier, it is important to analyze how those metrics change depending on the chosen increment size. As an initial case study, consider a target wall geometry of 6.35 mm wide and 30 mm tall, and assume, for simplicity, that it is possible to build the target geometry in either 5-, 10-, 15-, or 30-mm increments. The production time to deposit and machine the entire geometry in the given increments and the BTF ratio for each increment size are calculated for each interlayer dwell time strategy.

Figure 15b shows that when the constant 60-s interlayer dwell time strategy is used, the production time decreases as the increment size increases. Note that the production time for experiment 1 decreases by approximately 600 s, but the production times for experiments 2 and 3 only decrease by 200–300 s. This is due to the fact that experiment 1 has a larger excess area profile as in Fig. 14a. The BTF in Fig. 15a, on the other hand, only shows a marginal increase of 0.01 to 0.05 as the increment size increases, with experiment 2 having the lowest BTF values for all increment sizes. Another

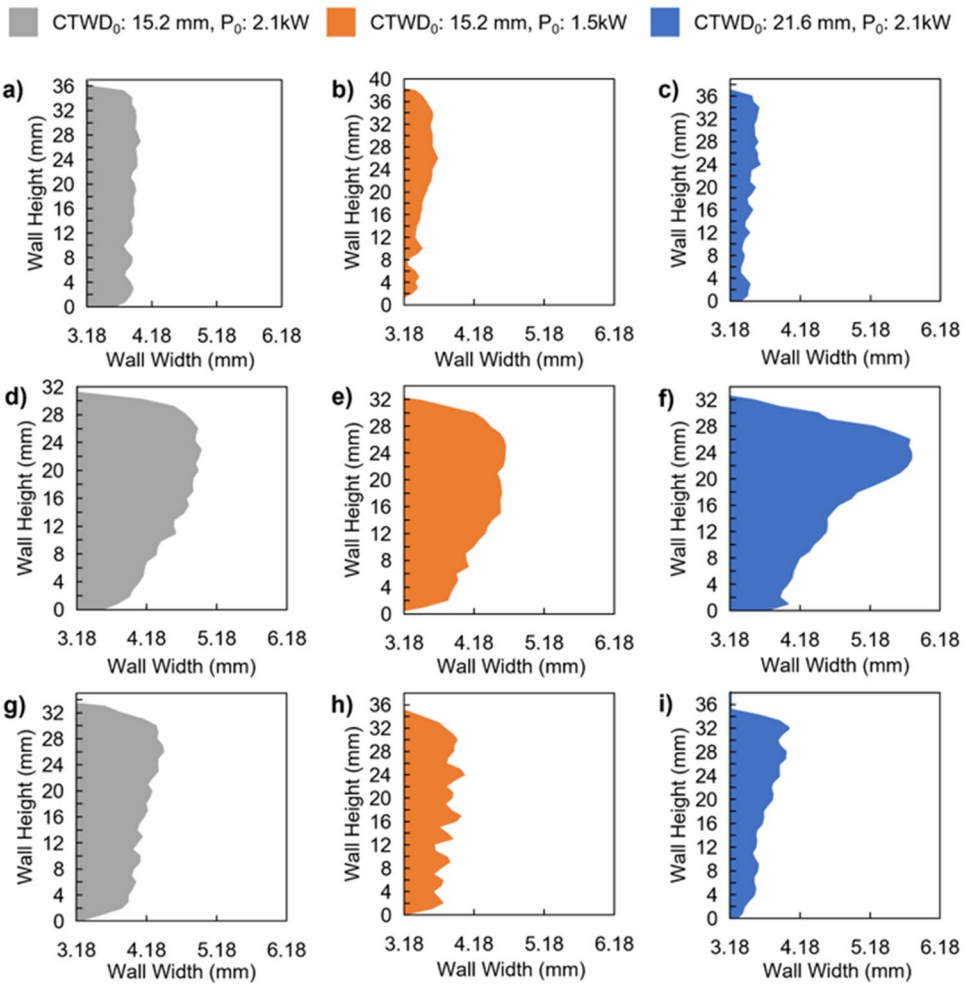

Fig. 14 Excess area profiles of as-deposited wall artifacts from (**a**) experiment 1, (**b**) experiment 2, (**c**) experiment 3, (**d**) experiment 4, (**e**) experiment 5, (**f**) experiment 6, (**g**) experiment 7, (**h**) experiment 8, (**i**) experiment 9

interesting observation is that the production time values for the 5-mm increment size have a range of approximately 600 s but converge to a range of approximately 150 s for the 30-mm increment size. When no interlayer dwell time is used, Fig. 15c and d show that there are similar trends seen for experiments 4, 5, and 6. Production time decreases by approximately 500 s to 700 s, and BTF increases by approximately 0.2 when the increment size increases. It should be noted that experiment 5 has the lowest BTF and production time values for all increment sizes. Additionally, the range in production time values stays relatively constant at 150–180 s from the 5-mm to the 30-mm increment size.

Lastly, Fig. 15e and f show the results for when the 0- or 60-s alternating dwell time strategy is used. The trends in production time and BTF are similar across experiments 7, 8, and 9, but experiment 7 has the largest decrease in production time of ~ 700 s, followed by experiment 8 with ~ 500 s and experiment 9 with ~ 250 s. This can be attributed to the differences in excess area profile as seen in Fig. 14g, h, and i. The range of production times decreases from approximately 600 to 150 s as the increment size increases from 5 to 30 mm. The BTF shows increases of approximately 0.07 to 0.11, which are slightly higher than those of the constant 60-s interlayer dwell condition. The case study shows that there are vast improvements that can be made to both production time and BTF by utilizing multiple incremental deposition and machining operations as opposed to only doing one deposition and machining operation to reach the target geometry. What complicates this approach is the selection of the right increment size. As shown in this case study, there are tradeoffs between the production time and BTF ratio that are dependent on the increment size. Manufacturers must therefore integrate their own unique considerations of production time and BTF when making this decision.

6 Conclusions

In this paper, several wall depositions are conducted where dwell time, P_0, and $CTWD_0$ are varied. A data collection architecture for a retrofit WAAM system is described that is used to measure current and voltage data from the welding

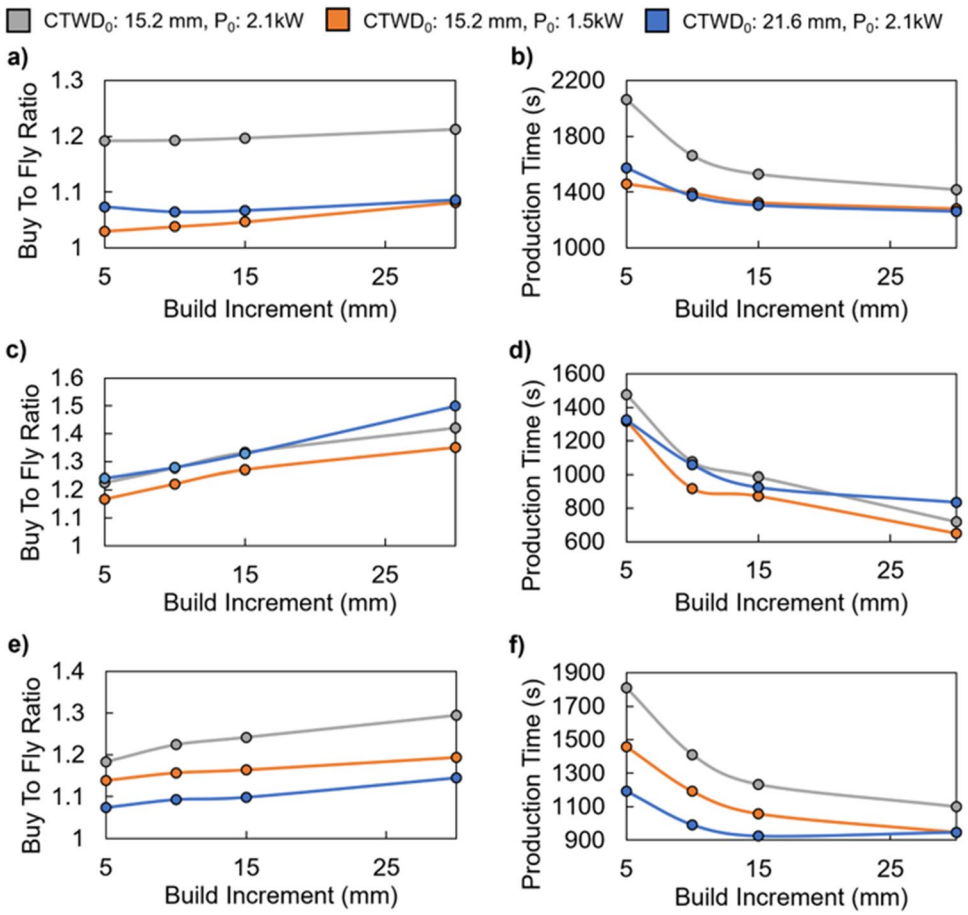

Fig. 15 Case study production metric graphs: (**a**) BTF for 60-s dwell time, (**b**) production time for 60-s dwell time, (**c**) BTF for 0-s dwell time, (**d**) production time for 0-s dwell time, (**e**) BTF for 0–60-s alternating dwell time, (**f**) production time for 0–60-s alternating dwell time

power supply, and images of the welding process are taken in situ to monitor the $CTWD_a$. An average value for the current, voltage, P_a, and $CTWD_a$ is found for each layer, and the resulting walls are scanned with a laser line scanner to determine average wall height and width. The overall production time, consisting of the deposition and machining time, is then calculated from the resulting wall geometry as well as the BTF ratio. Additionally, a case study is conducted to analyze the effects of using multiple incremental deposition and machining operations to reach a target geometry on the production time and BTF ratios. Those two metrics are calculated for several different increment sizes for each wall artifact. The following conclusions can be drawn from the resulting analysis of the process data:

- Both measured welding current and $CTWD_a$ calculated from welding images are suitable data streams for determining the part height in situ and vary from the high-fidelity geometric scans by less than 6%.
- Using lower P_0 or increased $CTWD_0$, 60-s and 0–60-s alternating dwell time trials resulted in 0.34-mm deviation in average width and 0.63-mm deviation in average height due to different bead penetration and power levels for parameter sets.
- Decreasing dwell time increases the percentage of the overall production time needed for machining (8–12% for 60-s dwell time, 17–22% for 0- or 60-s alternating dwell time, and 45–58% for 0-s dwell time) but decreases the overall production time (~ 1800s for 60-s dwell time, ~ 1300 s for 0- or 60-s alternating dwell time, ~ 900 s for 0-s dwell time).
- Using lower P_0 or increased $CTWD_0$, 0- or 60-s alternating dwell time trials reduced production time by ~ 30% while only underbuilding the desired wall geometry by ~ 2%.
- The 0-s dwell time trials had the fastest production rate in terms of the finished wall production rate (1.97–2.55 mm in Z/min) but the highest BTF ratio values (1.34–1.48).
- The case study showed that the finished wall production time and BTF ratio are dynamic depending on the increment chosen and on the dwell time strategy employed.

Author contribution Conceptualization: Austen Thien, Christopher Saldana. Methodology: Austen Thien. Software: Austen Thien. Validation: Austen Thien, Christopher Saldana, Thomas Kurfess. Formal

analysis: Austen Thien. Investigation: Austen Thien. Resources: Austen Thien, Christopher Saldana, Thomas Kurfess. Data curation: Austen Thien. Writing—original draft preparation: Austen Thien. Writing—review and editing: Thomas Kurfess, Christopher Saldana. Supervision, Thomas Kurfess, Christopher Saldana. Project administration: Thomas Kurfess, Christopher Saldana. Funding acquisition: Thomas Kurfess, Christopher Saldana. All authors have read and agreed to the published version of the manuscript.

Funding This work was supported by the US Department of Energy DE-EE0008303 and an NDSEG fellowship to Austen Thien.

Availability of data and material All data is available upon request to the corresponding author.

Declarations

Ethics approval Not applicable.

Consent to participate Not applicable.

Consent for publication Not applicable.

Competing interests The authors declare no competing interests.

References

1. Rodrigues TA, Duarte V, Miranda RM, Santos TG, Oliveira JP (2019) Current status and perspectives on wire and arc additive manufacturing (WAAM). Materials 12:1121–1163. https://doi.org/10.3390/ma12071121
2. Geng H, Li J, Xiong J, Lin X, Huang D, Zhang F (2018) Formation and improvement of surface waviness for additive manufacturing 5A06 aluminium alloy component with GTAW system. Rapid Prototyp J 24:342–350. https://doi.org/10.1108/RPJ-04-2016-0064
3. Kumar A, Maji K (2020) Selection of process parameters for near-net shape deposition in wire arc additive manufacturing by genetic algorithm. J Mater Eng Perform 29:3334–3352. https://doi.org/10.1007/s11665-020-04847-1
4. Abedayo A, Mehnen J, Tonnellier X (2012) Limiting travel speed in additive layer manufacturing. 9th International Conference on Trends in Welding Research
5. Yehorov Y, da Silva LJ, Scotti A (2019) Balancing WAAM production costs and wall surface quality through parameter selection: a case study of an Al-Mg5 alloy multilayer-non-oscillated single pass wall. J Manuf Mater Process 3:32–51. https://doi.org/10.3390/jmmp3020032
6. Kohler M, Hensel J, Dilger K (2020) Effects of thermal cycling on wire and arc additive manufacturing of Al-5356 components. Metals 10:952–963. https://doi.org/10.3390/met10070952
7. da Silva LJ, Souza DM, de Araujo DB, Reis RP, Scotti A (2020) Concept and validation of an active cooling technique to mitigate heat accumulation in WAAM. Int J Adv Manuf Technol 107:2513–2523. https://doi.org/10.1007/s00170-020-05201-4
8. Li F, Chen S, Shi J, Zhao Y, Tian H (2018) Thermoelectric cooling-aided bead geometry regulation in wire and arc-based additive manufacturing of thin-walled structures. Appl Sci 8:207–212. https://doi.org/10.3390/app8020207
9. Reisgen U, Sharma R, Mann S, Oster L (2020) Increasing the manufacturing efficiency of WAAM by advanced cooling strategies. Weld World 64:1409–1416. https://doi.org/10.1007/s40194-020-00930-2
10. Wang B, Yang G, Zhou S, Cui C, Qin L (2020) Effects of on-line vortex cooling on the microstructure and mechanical properties of wire arc additively manufactured Al-Mg alloy. Metals 10:1004–1019. https://doi.org/10.3390/met10081004
11. Kozamernik N, Bracun D, Klobcar D (2020) WAAM system with interpass temperature control and forced cooling for near-net-shape printing of small metal components. Int J Adv Manuf Technol 110:1955–1968. https://doi.org/10.1007/s00170-020-05958-8
12. Lee S (2020) Optimization of cold metal transfer-based wire arc additive manufacturing processes using Gaussian process regression. Metals 10:461–474. https://doi.org/10.3390/met10040461
13. Fuchs C, Baier D, Semm T, Zaeh M (2020) Determining the machining allowance for WAAM parts. Prod Eng 14:629–637. https://doi.org/10.1007/s11740-020-00982-9
14. Xiong J, Yin Z, Zhang W (2016) Closed-loop control of variable layer width for thin-walled parts in wire and arc additive manufacturing. J Mater Process Technol 233:100–106. https://doi.org/10.1016/j.jmatprotec.2016.02.021
15. Reisgen U, Mann S, Oster L, Lozano P, Sharma R (2019) Study on workpiece and welding torch height control for polydirectional WAAM by means of image processing. IEEE 15th International Conference on Automation Science and Engineering
16. Xiong J, Zhang J, Pi Y (2020) Control of deposition height in WAAM using visual inspection of previous and current layers. J Intell Manuf. https://doi.org/10.1007/s10845-020-01634-6
17. Heralic A, Christiansson A, Lennartson B (2012) Height control of laser metal-wire deposition based on iterative learning control and 3D scanning. Opt Lasers Eng 50:1230–1241. https://doi.org/10.1016/j.optlaseng.2012.03.016
18. Silva RHG, dos Santos Paes LE, Barbosa RC, Sartori F, Schwedersky MB (2018) Assessing the effects of solid wire electrode extension (stick out) increase in MIG/MAG welding. J Braz Soc Mech Sci 40:31–38. https://doi.org/10.1007/s40430-017-0948-9
19. Henckell P, Gierth M, Ali Y, Reimann J, Bergmann JP (2020) Reduction of energy input in wire arc additive manufacturing (WAAM) with gas metal arc welding (GMAW). Materials 13:2491–2509. https://doi.org/10.3390/ma13112491
20. Scetinec A, Klobcar D, Bracun D (2021) In-process path replanning and online layer height control through deposition arc current for gas metal arc based additive manufacturing. J Manuf Process 64:1169–1179. https://doi.org/10.1016/j.jmapro.2021.02.038
21. Aldalur E, Veiga F, Suarez A, Bilbao J, Lamikiz A (2020) Analysis of the wall geometry with different strategies for high deposition wire arc additive manufacturing of mild steel. Metals 10:892–910. https://doi.org/10.3390/met10070892
22. Xia C, Pan Z, Polden J, Li H, Xu Y, Chen S, Yuming Z (2020) A review on wire arc additive manufacturing: monitoring, control, and a framework of automated system. J Manuf Syst 57:31–45. https://doi.org/10.1016/j.jmsy.2020.08.008
23. Mosavi A, Fatemeh S, Laszlo N, Karoly S, Gorji N (2020) Modeling the temperature distribution during laser hardening processes. Results Phys 16. https://doi.org/10.1016/j.rinp.2019.102883
24. Ding D, Pan Z, Cuiuri D, Li H, van Duin S, Larkin N (2016) Bead modelling and implementation of adaptive MAT path in wire and arc additive manufacturing. Robot Comput Integr Manuf 39:32–42. https://doi.org/10.1016/j.rcim.2015.12.004
25. Xiong J, Li Y, Li R, Yin Z (2018) Influences of process parameters on surface roughness of multi-layer single pass thin-walled parts in GMAW-based additive manufacturing. J Mater Process Technol 252:128–136. https://doi.org/10.1016/j.jmatprotec.2017.09.020

26. Ibrahim IA, Mohamat SA, Amir A, Ghalib A (2012) The effect of gas metal arc welding (GMAW) processes on different welding parameters. International Symposium on Robotics and Intelligent Sensors
27. Barz A, Buer T, Haasis HD (2016) A study on the effects of additive manufacturing on the structure of supply networks. Int Fed Automat Control 49:72–77. https://doi.org/10.1016/j.ifacol.2016.03.013